

# Marine snow surface production and bathypelagic export at the Equatorial Atlantic from an imaging float

Joelle Habib<sup>1</sup>, Lars Stemmann<sup>1,6</sup>, Alexandre Accardo<sup>1</sup>, Alberto Baudena<sup>1</sup>, Franz Philip Tuchen<sup>2,3</sup>, Peter Brandt<sup>4,5</sup>, Rainer Kiko<sup>1,4,5</sup>

<sup>1</sup>Sorbonne Université, CNRS, Laboratoire d'Océanographie de Villefranche, LOV, 06230 Villefranche-sur-Mer, France

<sup>2</sup>Cooperative Institute for Marine and Atmospheric Studies, Rosenstiel School of Marine, Atmospheric, and Earth Science, University of Miami, Miami, FL, USA

<sup>3</sup>NOAA/Atlantic Oceanographic and Meteorological Laboratory, Miami, FL, USA

<sup>4</sup>GEOMAR Helmholtz Centre for Ocean Research Kiel, Kiel, Germany

<sup>5</sup>Faculty of Mathematics and Natural Sciences, Kiel University, Kiel, Germany

<sup>6</sup>Institut Universitaire de France (IUF), Paris, France

Correspondence to: Joelle Habib (joellehabib22@hotmail.com)

**Abstract.** The marine biological carbon pump (BCP) plays a central role in the global carbon cycle, transporting carbon from the surface to the deep ocean and sequestering it for long periods. Sinking of surface-produced particles, known as the Biological Gravity Pump (BGP) constitutes the main component of the BCP. To study the BGP in the equatorial Atlantic upwelling region, a biogeochemical (BGC) Argo float equipped with an Underwater Vision Profiler 6 (UVP6) camera was deployed from July 2021 to March 2022. The float was recovered after its eastward drift from 23°W to 7°W along the equator, during which it conducted profiles to 2000 m depth every three days. For the first time in this oceanic region, in situ images and physical and biogeochemical data from a BGC-Argo float were acquired and analyzed in combination with satellite data. During the float trajectory, two blooms were recorded followed by two main export events of sinking aggregates that lasted for over a month, consistently reaching 2000 m depth. A Lagrangian approach was applied to investigate the production, transformation, and deep export of marine particles. Based on the characterization of the morphology of detritus within and outside of the plumes, five particle morphotypes with different sinking properties were detected. Small and dense aggregates were present throughout the water column while porous morphotypes, despite being larger, were predominantly concentrated in the surface layer. Export was driven by small and compact particles with higher particle abundance and flux during upwelling and export events. Our investigation reveals the stability of the equatorial Atlantic BCP system during this period, yielding an export efficiency of 6–7% during and outside of export events. This study highlights the importance of using new technologies on autonomous platforms to characterize the temporal variability in the magnitude and functioning of the BCP.

## 1 Introduction

The term “biological carbon pump” (BCP) encompasses physical and biological processes responsible for the generation, export, and remineralization of organic matter from the upper ocean to depth (Boyd et al., 2019; DeVries et al., 2012; Steinberg & Landry, 2017). The biological pump connects various aspects of the carbon cycle: the upper-ocean photosynthetic carbon uptake, the alimentation of the midwater biota (Irigoien et al., 2014), and the carbon storage within the deep sea (Buesseler et al., 2007). Within the euphotic zone, organic particles are continuously generated and recycled, with only a small fraction descending into deeper layers (De La Rocha, 2004), while remineralization occurs within a few hundred meters of the surface and is facilitated by processes such as

zooplankton feeding or microbial degradation (Giering et al., 2014; Steinberg & Landry, 2017; Stemmann, Jackson, & Ianson, 2004). Given the retroactive potential of the BCP to significantly impact anthropogenic climate warming (Bernardello et al., 2014; Bopp et al., 2013), understanding the multitude of mechanisms governing the BCP is of paramount importance.

Among the different processes of the BCP, sinking marine snow is the key component of particulate carbon transport to the deep ocean, a process known as the biological gravitational pump (BGP). Marine snow consists of detritus, formed from a mixture of source particles produced by the surface ecosystem and aggregated together by physical (coagulation) or biological (trophic activity) mechanisms (Alldredge & Silver, 1988). Their composition is determined by multiple characteristics, mainly the phytoplankton and zooplankton community composition (Bach et al., 2019; Tréguer et al., 2018). In the mesopelagic layers, several biological and physical factors influence their dynamics and control their size distribution and morphology, which affect their sinking (Cael et al., 2021; Stemmann, Jackson, & Ianson, 2004). Shear and differential settling modulates aggregation (Jackson, 1990; Stemmann et al., 2004) while fragmentation rates have been proposed to depend on shear and swimming organisms (Briggs et al., 2011; Dilling & Alldredge, 2000; Jackson, 1990). Additionally, particle volume and surface area condition interactions with microorganisms (e.g., colonization and degradation of particles; Bianchi et al., 2018), modifying marine snow morphology by making them more porous and fragile with time (Biddanda & Pomeroy, 1988; Ploug & Grossart, 2000). Mineral ballasting, through the association of marine snow with dense inorganic materials such as calcium carbonate, lithogenic or biogenic silica, can also significantly enhance sinking velocities and control the carbon export efficiency (Armstrong et al., 2001; Klaas and Archer, 2002).

Formatted: English (UK)

An efficient tool to track the particle morphology, study their abundance, and estimate the vertical carbon flux is the Underwater Vision Profiler (UVP; Picheral et al., 2010, 2022). This imaging tool measures particle abundance and distribution (Guidi et al., 2009; Kiko et al., 2022; Stemmann et al., 2002), to estimate the biological gravitational pump (Forest et al., 2013; Guidi et al., 2015; Kiko et al., 2017; Ramondenc et al., 2016), and more recently, to explore particle morphology (Trudnowska et al., 2021; Accardo et al., submitted). One decade of observation with the UVP5 during ship surveys allowed a global monitoring (Forest et al., 2013; Guidi et al., 2008, 2015; Kiko et al., 2017; Stemmann et al., 2002) and enabled the reconstruction of global export fluxes from the spatially variable euphotic zone and mixed layer depths (Clements et al., 2022, 2023; Guidi et al., 2015).

Despite significant improvement in observation capacities from ships, high frequency observations during long-term deployment to study relevant scales of marine snow dynamics over a large depth range was not possible. Autonomous platforms equipped with imaging sensors have emerged and are currently being utilized to remotely record plankton and particle distributions in addition to the core parameters such as salinity, temperature, and optically derived other variables (Claustre et al., 2020; Picheral et al., 2022). Recently, surface blooms followed by plumes of sinking material were monitored using optical sensors (fluorescence and backscatter) mounted on BGC-Argo float drifting in a quasi-Lagrangian mode (Briggs et al., 2011, 2020) and global POC standing stocks have been calculated (Fox et al., 2024). Such studies with optical sensors (fluorescence, backscatter) are key to understanding particle dynamics in the core of the oceans but they are not adapted to study marine snow.

We selected the equatorial Atlantic Ocean to conduct our study, as it is characterized by enhanced primary productivity concentrated within the equatorial and coastal regions (Grotsky et al., 2008). This productivity is due

to the presence of upwelling zones in the central and eastern parts of the equatorial basin (Schott et al., 1998) which bring nutrients to the euphotic zone (Radenac et al., 2020). This enhanced productivity results in a stronger passive and active export of particulate matter reaching up to 4000 m (Kiko et al., 2017). The strength of the equatorial upwelling system is modulated by the strength of seasonally varying winds associated with the meridional migration of the intertropical convergence zone (Brandt et al., 2023). At intraseasonal (20-50 days) scales, Tropical Instability Waves (TIWs) are another factor influencing the equatorial local productivity. TIWs are westward-propagating, cusp-shaped oscillations prevalent in the central and western equatorial Atlantic generated by baroclinic and barotropic instabilities (Athie & Marin, 2008). They induce strong intraseasonal variations in sea surface temperature, sea surface salinity, and ocean currents (Tuchen et al., 2022), and are associated with sharp fronts (Warner et al., 2018). TIWs can also influence nitrate (Radenac et al., 2020) and chlorophyll distribution (Menkes et al., 2002; Sherman et al., 2022).

We here focus on the equatorial Atlantic BGP, using data from a UVP6 camera mounted on a BGC-Argo float deployed at 23°W, 0° in July 2021 to study the impact of seasonal upwelling and intraseasonal TIWs on productivity and particle export. In particular, we use a plume-based approach to follow the initiation and vertical extent of export events, to characterize particle production of various morphotypes during two bloom events, and to describe the patterns of their attenuation as they are exported to the meso- and bathypelagic layers.

## 2 Material and Methods

### 2.1 Satellite data

#### 2.1.1 Sea surface chlorophyll-a

Estimates of chlorophyll-a (chl-a) concentration and anomalies for the tropical Atlantic were obtained from the combination of two different products: the Global Ocean Color product (OCEANCOLOUR\_GLO\_BGC\_L4\_MY\_009\_104) produced by ACRI-ST and the NOAA-VIIRS provided by NOAA CoastWatch. Both of these data sets provide gap-free time series, with a temporal extent from 1997 till 2023 for the first product, while the second one only started in 2018. The temporal resolution for both products is one day with a spatial resolution of 4 km for the first product and 9 km for the second one.

#### 2.1.2 Sea surface temperature

Sea surface temperature (SST) and SST anomaly data were downloaded from the NOAA OI-SST data set (Huang et al., 2021; <https://psl.noaa.gov/data/gridded/data.noaa.oisst.v2.highres.htm>). SST anomalies are computed relative to a 30-year climatological mean. The gridded data are available daily from 1981-present at a horizontal resolution of 0.25°. To isolate TIW induced SST variability from the time series, a temporal (20-50 days) and a zonal (4-20° wavelength) bandpass filter were applied in accordance with previous studies (Olivier et al., 2020; Tuchen et al., 2022).

#### 2.1.3 Lagrangian diagnostics

Several Lagrangian diagnostics were computed for each sampling station using velocity data and environmental satellite products. To this aim, we defined for each station a circular region that we consider representative of the water parcel sampled by the BGC-Argo float. A radius of 0.1° was used (consistently with previous studies, Baudena et al., 2021; Fabri-Ruiz et al., 2023; Ser-Giacomi et al., 2021), and the circular region was filled with

115 virtual particles. A given diagnostic is calculated for each virtual particle in the circular region. These values are  
116 then averaged together, providing one value of a given diagnostic per station.

117 The velocity field used is the Copernicus CMEMS product MULTIOBS GLO PHY REP 015 004-TDS at 15 m  
118 depth. This product has a spatial resolution of 0.25° and a daily temporal resolution. It is derived from satellite  
119 altimetry and model assimilation and includes both geostrophic and Ekman components. Using the surface velocity,  
120 each particle within the circular region of a given sampling station was advected using a Runge-Kutta scheme of  
121 order 4 from the day of the sampling backward in time. Different advective times were used, from 5 to 45 days.

122 Two types of diagnostics were carried out: Eulerian and purely Lagrangian diagnostics. These groups consist of  
123 calculating properties that are integrated in time: at the sampling location (Eulerian) or along the trajectory of the  
124 water parcel (Lagrangian). In this study, we only present diagnostics that are relevant to our area of study, such as  
125 the Lagrangian and Eulerian chl-a, divergence, and vorticity. The Lagrangian chlorophyll, the average chl-a content  
126 carried by the water parcel in the previous days, provides information on the recent primary productivity. The  
127 Lagrangian divergence can be considered as a proxy of the upwelling (when negative) or downwelling (when  
128 positive) experience by the water parcel in the previous days. This metric has been correlated with chlorophyll  
129 (Hernández-Carrasco et al., 2018).

130 In the following, we will report diagnostics calculated using an advective time of 15 days. This value was chosen  
131 as it showed the highest correlations between the chl-a concentrations and the abundance of micrometric particles  
132 and macroscopic particles between 0-100m (Supplementary Fig. S8).

## 133 2.2 Float data

### 134 2.2.1 Coverage and data collection

135 For this study, a BGC-Argo float (WMO:6904139) was deployed at the equator during *RV Sonne* SO284 cruise  
136 traversing the transect from 23°W to 7°W migrating from west to east during the period between July 2021 and  
137 March 2022. The float was recovered during the PIRATA FR32 cruise. This float was equipped with several  
138 physical and biogeochemical sensors to measure the pressure, temperature, salinity, chlorophyll, oxygen, and  
139 particle backscattering coefficient (BBP, measured at 700 nm) with a vertical resolution of 5 m. BGC-Argo float  
140 data were collected through the International Argo Program and can be found at <https://argo.ucsd.edu>. Chl-a and  
141 BBP both present a gap between the 1<sup>st</sup> and the 5<sup>th</sup> of January 2022.

### 142 2.2.2 UVP measurements

143 An Underwater Vision Profiler 6 (UVP6) was mounted on the BGC Argo float. This camera-based particle counter  
144 sizes and counts marine particles (Kiko et al., 2022) covering a size range from 0.102 mm to 16.4 mm. The UVP  
145 contributes to understanding sinking organic particles and carbon sequestration at global (Guidi et al., 2015) and  
146 regional scales (Ramondenc et al., 2016). More information about calibration and data processing can be found in  
147 Picheral et al. (2021). In total, our data set includes 86 profiles reaching at least 1000 m. Every 3 days, the BGC  
148 Argo float reached 2000 m. According to the recorded profiling times, at least 50% of the profiles were conducted  
149 during nighttime, with many occurring close to local midnight. For all parameters, we interpolated the data set with  
150 a vertical resolution of 10 m and a temporal resolution of a day.

Deleted:

### 152 2.2.3 Mixed layer depth calculation

153 To determine the mixed layer depth, we use temperature profiles provided by the BGC-Argo float. Using the  
154 definition outlined in De Boyer Montégut et al. (2004), the mixed layer was determined by identifying the depth at  
155 which the temperature decreased by 0.2°C relative to the temperature at 10 m depth. The mixed layer depth in this  
156 study reached a depth of 60 m.

Deleted:

### 157 2.2.4 Particle abundance and carbon flux calculation

158 Particle size abundances (number of particles per liter) for depth bins of 2.5 m along the water column were  
159 obtained by the UVP. Particles were divided into two categories based on their size: Micrometric particles (MiP)  
160 for particles ranging between 0.1-0.5 mm, and Macroscopic particles (MaP) ranging between 0.5-16 mm. The  
161 carbon flux was obtained by integrating all size classes and therefore represents the total carbon flux. To calculate  
162 the flux for a given size class, we used the relationship provided by Kriest (2002), linking the particle size to the  
163 sinking speed and its carbon content. This relationship has been used in former studies using UVP observations  
164 (Kiko et al., 2017). For each parameter, we interpolated the profiles in depth with a vertical resolution of 10 m and  
165 a temporal resolution of a day.

### 166 2.2.5 Determination of export events

167 We determined periods of export events, using the anomalous carbon flux. We calculated the total mean particle  
168 abundance and mean carbon flux along the water column from the interpolated fields for the deployment period.  
169 The resulting mean profile was then subtracted from the individual particle abundance and carbon flux profiles,  
170 yielding anomaly profiles. This helped us determine two different types of periods: periods with main export events  
171 and periods where no or weak export occurred.

### 172 2.2.6 Regime shift detection for surface export

173 A sequential algorithm for regime shift detection (Rodionov, 2004) was applied to the MaP abundance for the first  
174 200 m to identify accurately the beginning and the end of the carbon export events. This method identifies  
175 discontinuities in a time series without prior assumptions of the timing of the regime shifts. The algorithm requires  
176 a set of parameters to specify: the target significance level and the cutoff length. The target significance used here  
177 is  $p=0.05$ . The cutoff length affects the time scale of the regime by removing regimes of shorter duration than the  
178 reference value. In this study, the cutoff length was set to 9 days to cover at least 3 profiles. For more details, see  
179 Rodionov (2004, 2006). We determined three masks, two corresponding to periods of export 'event 1', 'event 2',  
180 and a period where no main export plume was observed, hereafter referred to as the 'outside-between' mask. It  
181 should be noted that 'outside-between' refers to periods that do not belong to the two main export events.

Deleted:

### 182 2.2.7 Morphological properties of detritus

183 The data set consisted of 127,000 images. Each image underwent individual classification using the Ecotaxa  
184 program with the support of machine learning classifiers (Picheral et al., 2017). This classification differentiates  
185 between living and non-living organisms. The automatically classified images were then manually validated or  
186 reclassified. To distinguish between different types of marine snow, we examined the morphological properties of  
187 individual objects such as size (area, perimeter), shade intensity (mean/median gray level), shape (elongation), and

structural complexity (homogeneity or heterogeneity of gray levels). This was done using a principal component analysis (Fig. S6) to summarize the morphological information into a few new variables, followed by k-means clustering to separate different morphotypes of particles (Trudnowska et al. 2021). Using this method, we distinguish between five types of marine snow, as this number was a good compromise between the continuum of change in morphology and a need for simplicity. Concentration in numbers (numbers m<sup>-3</sup>) was computed per 10 m bins for each UVP6 profile.

### 2.2.8 Flux attenuation and biological carbon pump efficiency

The biological carbon pump (BCP) was computed following Engel et al. (2023), and Buesseler et al. (2020):

$$BCP = E_{eff} \times T_{eff} \quad (1)$$

With E<sub>eff</sub>, as the carbon export efficiency (E<sub>eff</sub>)

$$E_{eff} = \frac{F_{Z0}}{PP} \quad (2)$$

F<sub>Z0</sub> is the carbon export flux out of the surface ocean layer, corresponding to 100 m. While PP is the amount of CO<sub>2</sub> fixed by primary production, both in mg m<sup>-3</sup> d<sup>-1</sup>. Satellite-based net primary production (NPP) was downloaded from the Ocean Productivity website ([www.science.oregonstate.edu/ocean.productivity](http://www.science.oregonstate.edu/ocean.productivity)) using the Vertically Generalized Production Model (VGPM)-Eppley.

T<sub>eff</sub> represents the carbon transfer efficiency:

$$T_{eff} = \frac{F_Z}{F_{Z0}} \quad (3)$$

F<sub>Z</sub> is the flux at a particular depth and Z<sub>0</sub> is the reference depth (taken here as 100 m). T<sub>eff</sub> is related to the attenuation of carbon flux with depth, over 0-1000 m, quantified by a Martin power law (Martin et al., 1987).

$$F_Z = F_{Z0} \times \left(\frac{Z}{Z_0}\right)^{-b} \quad (4)$$

Z is the depth. The exponent b represents the attenuation with depth. An analogous equation was used to describe the particle attenuation.

$$n_Z = n_{Z0} \times \left(\frac{Z}{Z_0}\right)^{-b} \quad (5)$$

n<sub>Z</sub>, n<sub>Z0</sub> are the concentrations of particles at depth Z or Z<sub>0</sub>.

## 3 Results

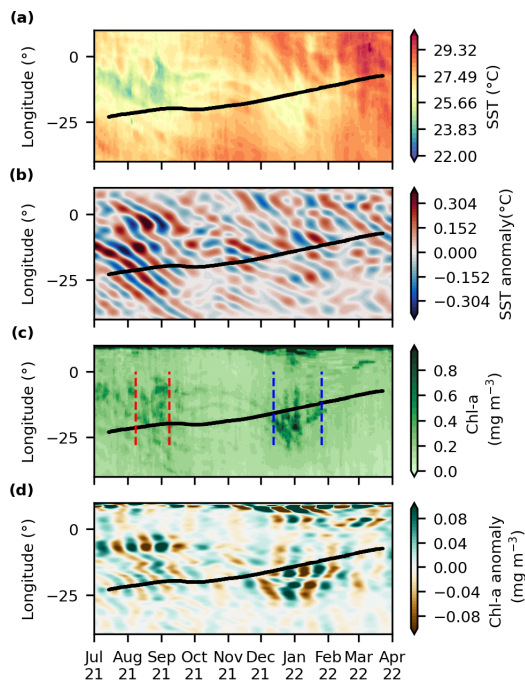
### 3.1 Satellite data analysis

Throughout the float trajectory (Fig. S1), satellite observations disclosed the presence of relatively cold surface waters during two distinct periods: August-October 2021 and December 2021 to February 2022 (Fig. 1a). The first period aligned with the seasonal development and peak of the Atlantic cold tongue with minimum surface temperatures around 23.8°C. The second period was from December to February with temperatures around 26°C.

220 The seasonal surface warming occurring between October and December featured values reaching 27.5°C, while  
 221 temperatures reached almost 29.5 during March and April (Fig. S2a). The temperatures were warmer than usual  
 222 compared to the climatology from 2012-2022, especially throughout the boreal summer of 2021 (Fig. S2a).

223 Before and during the cold tongue development in July to September 2021, bandpass-filtered SST anomalies  
 224 oscillated between -0.3°C and 0.3°C and showed westward propagation (Fig. 1b), suggesting the presence of TIWs.  
 225 A weaker TIW signal was observed during the second period when SST anomalies ranged between -0.1°C and  
 226 0.1°C.

227 Peaks of chl-a were observed during both low-temperature periods reaching about 0.4 mg m<sup>-3</sup> on 10 September  
 228 2021 and 2 January 2022 (Fig. 1c, S2b). The surface chl-a concentration ranged between 0.1 and 0.4 mg m<sup>-3</sup> along  
 229 the float trajectory. When comparing the chl-a to the climatology, a delay in both peaks was observed (Fig. S2b)  
 230 with a low peak during summer 2021 and a second high peak during winter 2022 for the float compared to the  
 231 climatology. The bandpass-filtered chl-a anomaly oscillated between -0.04 mg m<sup>-3</sup> and 0.04 mg m<sup>-3</sup> from August  
 232 to October (Fig. 1d). These anomalies seem to be anti-correlated with the SST anomalies (Fig. S2 c,d). However,  
 233 westward propagation of bandpass-filtered chl-a anomalies is less obvious than for SST. From December to March,  
 234 more pronounced chl-a anomalies were observed.



235

236 **Figure 1: Satellite-derived properties as a function of time (x-axis) and longitude (y-axis): (a) sea surface temperature**  
 237 **(°C), (b) bandpass-filtered sea surface temperature anomaly, (c) surface chl-a concentration (mg m<sup>-3</sup>), and (d) bandpass-**  
 238 **filtered chl-a anomaly along the equator from July 2021 to March 2022. The black line represents the float trajectory**

239 from west to east. The blue and red lines determine the beginning and the end of the first and the second export event,  
240 respectively.

## 241 3.2 Float data analysis

### 242 3.2.1 Physical parameters (Temperature, Salinity, mixed layer)

243 During August, the mixed layer depth (MLD) was at about 42 m, salinity integrated over the first 100 m showed a  
244 maxima of 36 PSU (Fig. 2a, S3a) while temperature (averaged over the top 100 m) showed a first minimum of  
245 21°C (Fig. 2b). Average 100-m temperature increased with the progressive deepening of the ML from September  
246 to January. MLD reached a maximum of 60 m in October. Salinity was high during the same period with a  
247 maximum of 36 psu in November (Fig. 2a). A second 100-me temperature minimum of 18.8°C was also recorded  
248 in January coinciding with the shoaling of the Deep Chlorophyll Maximum (DCM) and the presence of a salinity  
249 minimum in the top 100 m (Fig 2a,b, S3a,b). A subsurface maximum was determined for the salinity between 50-  
250 100 m (Fig. 2a,b). The thermocline, represented by the 20°C isotherm (black line, Fig. 2,e) was unusually deep  
251 during summer (80 m) compared to the Argo climatology and reached a maximum of 100 m in October. It was  
252 also unusually shallow (50 m) in January 2022.

### 253 3.2.2 Biogeochemical parameters (chl-a, BBP, oxygen)

254 The chl-a concentration reported by the BGC-Argo float in the first 100 m, varied between 0 and 0.5 mg m<sup>-3</sup>. Peaks  
255 reached 0.45-5 mg m<sup>-3</sup> values on September 18, November 3, and 8 December (Fig. 2d, S3a). Elevated chl-a  
256 concentrations were observed at 70 m depth, corresponding to the depth of the deep chl-a maximum. These values  
257 varied between 0.28 and 0.8 mg m<sup>-3</sup>. Both satellite and float chl-a data show the presence of two blooms (Fig. S3a).  
258 However, float data presented a more variable chl-a concentration compared to the satellite. This can be attributed  
259 to the low resolution of satellite images compared to the float and the interpolation methods applied to ensure a  
260 gap-free time series, but also to fundamental differences in how chl-a is measured. Float-based chl-a is derived  
261 from fluorescence and is sensitive to phytoplankton physiology, community composition, nutrient availability, and  
262 environmental conditions, whereas satellite measurements rely on optical reflectance and are largely insensitive to  
263 these factors (Long et al., 2024). BBP POC, calculated using a BBP-to-carbon relationship (Koestner et al., 2022),  
264 followed the same pattern as chl-a and small particles were concentrated in the first 90 m (Fig. 2e). Periods of high  
265 chl-a were correlated with an increase in the BBP POC. Oxygen concentrations reached values around 189 µmol  
266 kg<sup>-1</sup> (Fig. 2c) in the mixed layer. Concentrations decreased with depth, with values below 134 µmol kg<sup>-1</sup> below 100  
267 m.

Deleted: .



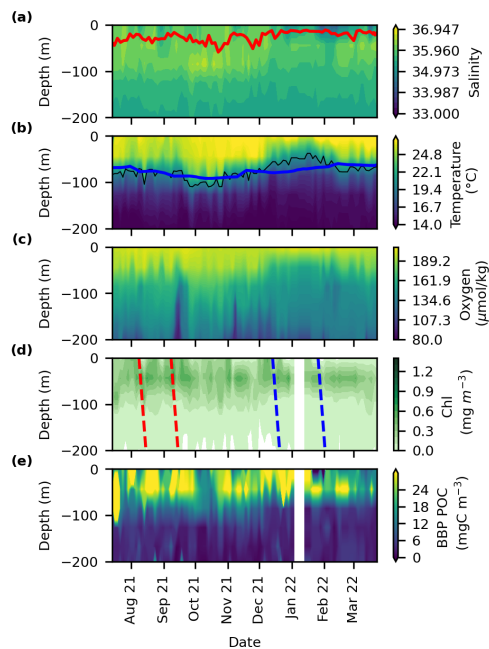


**Figure 2:** Time–depth profiles determined from the BGC-Argo float for (a) salinity, (b) temperature (°C), (c) oxygen ( $\mu\text{mol kg}^{-1}$ ), (d) chl-a ( $\text{mg m}^{-3}$ ) (e) and BBP POC ( $\text{mgC m}^{-3}$ ). The red line in (a) represents the mixed layer depth defined as a decrease of  $0.2^\circ\text{C}$  relative to temperature at 10 m depth. The black line in (b) represents the  $20^\circ\text{C}$  isotherm depth which is a well-known proxy for the thermocline in the tropics. The blue line in (b) is the average depth of the  $20^\circ\text{C}$  isotherm from the Argo climatology (2012 to 2022). The blue and red dashed lines in (d) determine the beginning and the end of the first and the second export event, respectively.

### 3.3 Carbon flux dynamics

#### 3.3.1 Surface flux and particle abundance along the trajectory (0-100m)

The increase in surface chl-a in the first 100 m was linked to an increase in surface carbon flux, MaP and MiP abundance (particles between 0.1-0.5 mm) (Fig. S3). All were significantly correlated with in situ chl-a ( $r^2=0.4$ ,  $0.6$  and  $0.3$ , respectively,  $p\text{-value}<0.01$ ). No significant correlation was found between surface chl-a and MaP abundance (particles  $>0.5$  mm). The highest integrated MiP abundance in the surface layer was recorded on the 18<sup>th</sup> of August 2021 with values reaching  $316 \text{ particles L}^{-1}$  (Fig. 3a,c, S3d). This also coincided with the highest MaP abundance with around  $5 \text{ particles L}^{-1}$ . Simultaneously with the surface chl-a peak, on 3 November 2021 a peak of MiP with  $348 \text{ particles L}^{-1}$  was also observed (Fig S3d), while carbon flux increased after a 15 day delay reaching  $250 \text{ mg C m}^{-2} \text{ day}^{-1}$  (Fig. S3f). The peak of chl-a, in December 2021 caused an increase in carbon flux, MiP, and MaP abundance.

#### 3.3.2 Flux and particle abundance pattern along the water column (averaged profile)

Throughout the float trajectory, the UVP6 data showcased high variability in MiP and MaP abundance, and carbon flux in the upper 100 m, with a dominance of small particles compared to big particles (Fig. 4a, S3). MiP and MaP increased in the surface layer peaking at 30-40 m, respectively. The maximum carbon flux,  $104.1 \pm 61.5 \text{ mgC m}^{-2}$

Deleted: Both

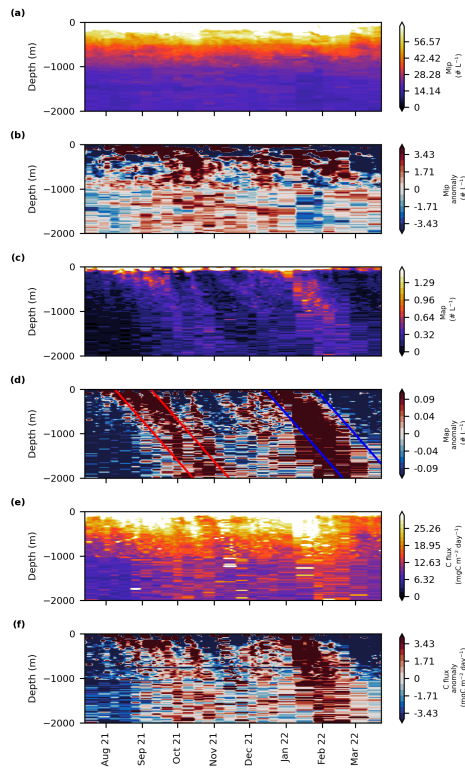
Formatted: English (UK)

Deleted: <sup>3</sup>

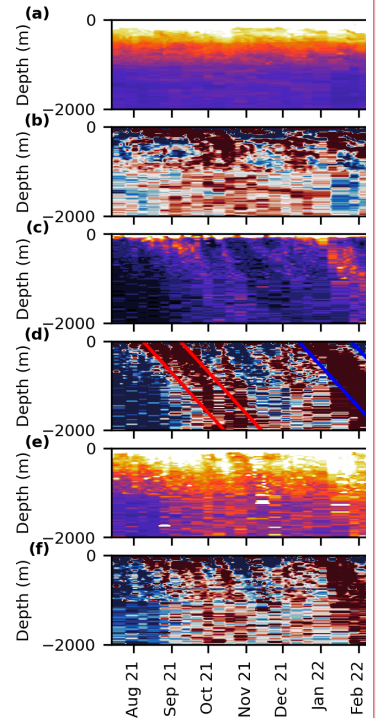
293 day<sup>-1</sup>, coincided with the MaP's maximum. After the surface layer peaks, MiP abundance and carbon flux declined  
294 rapidly until 1000 m, reaching  $22.5 \pm 1.3$  particles L<sup>-1</sup> and  $13.2 \pm 2.9$  mgC m<sup>-2</sup> day<sup>-1</sup>, while MaP's abundance  
295 decreased rapidly until 200 m with  $0.3 \pm 0.2$  particles L<sup>-1</sup>. Flux and abundance declined further with depth. The  
296 carbon flux was dominated by MiP abundance and followed its pattern.

297 **3.3.3 Evaluation of export events**

298 To investigate two settling plumes depicted in Figure 3d, four spaced lines were drawn on the MaP abundance with  
299 a slope of 30 m day<sup>-1</sup>, as suggested by Stemmann, Jackson, & Gorsky, (2004) using a model for particle size  
300 distribution. In reality, the plumes contain different types of sinking particles with varying velocities. Although the  
301 second plume appears to exhibit a higher sinking speed, particle composition does not change between the plumes.  
302 Therefore, to maintain consistency across all events, the same 30 m day<sup>-1</sup> criterion was applied throughout. The  
303 periods of surface production and export were determined using the Rodionov algorithm (Fig. S4). The first export  
304 event, “Event 1”, started at the surface on the 8th of August and lasted until the 8th of September 2021, while the  
305 second event, “Event 2”, occurred from the 13th of December 2021 to the 26th of January 2022. Both events lasted  
306 one month (Fig. 3f). These events are easily discernible on the MaP abundance and carbon flux plots as two plumes  
307 that reach 2000 m depth (Fig. 3c-f) while they are less visible in the MiP pattern.



Deleted: <sup>3</sup>



Deleted:

Figure 3: Time series of (a) MiP abundance ( $\# \text{ L}^{-1}$ ), (b) MiP anomaly, (c) MaP abundance ( $\# \text{ L}^{-1}$ ), (d) MaP anomaly, (e) carbon flux ( $\text{mgC m}^{-2} \text{ day}^{-1}$ ), and (f) carbon flux anomaly. The blue and red lines determine the beginning and the end of the first and the second export event, respectively.

Interestingly, the carbon flux profiles for events 1 and 2, and the ‘outside-between’ mask showed the same attenuation of the mean carbon flux along the water column (Fig. 4a,b). Flux at 30 m depth reached 168, 139, and 83  $\text{mg C m}^{-2} \text{ day}^{-1}$  for event 2, 1 and outside-between mask, respectively (Fig. 4a). The flux then decreased with depth during all periods. An intermediate particle maximum was observed for ‘outside-between’ and event 2 between 300-500 m (Fig. S5). The ‘outside-between’ mask showed the lowest carbon flux along the water column compared to the two export events. Flux during event 2 was the highest from 0-60 m and then from 120 m to 2000 m (Fig. 4a-c). Post hoc Tukey tests showed a significant difference between the outside-between mask and the two main export events for most of the layers of the water column (Fig. 4), while there was rarely a difference between events 1 and 2.

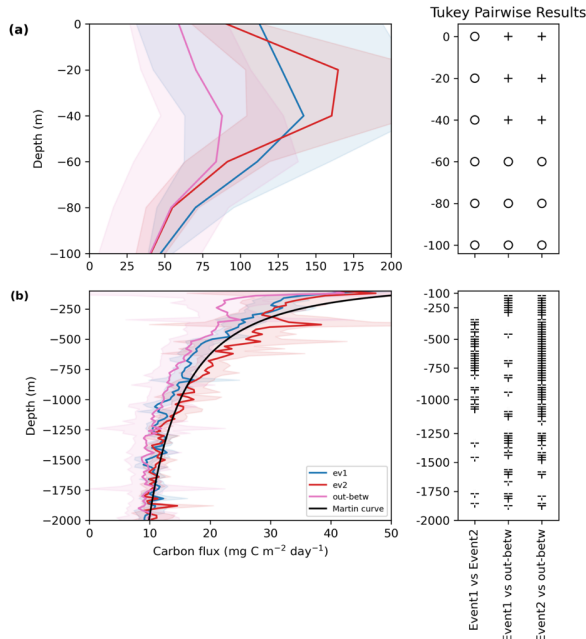


Figure 4: Averaged carbon flux profiles ( $\text{mg C m}^{-2} \text{ day}^{-1}$ ) along the plumes during event 1 (blue), event 2 (red), and the outside-between mask (purple) (a) from 0-100 m, (b) from 200-2000 m. The shading represents the standard deviation. The Tukey pairwise results were conducted for each depth. Plus signs indicate a significant difference, and blank space or empty circles indicate a non-significant difference. The black line represents the Martin curve of event 2 calculated using Eq. 4 with  $b=-0.6$  and  $F_{d0}=100\text{m}$ .

### 3.3.4 Flux attenuation and export efficiency

We parameterize the strength of the BCP pump using the export efficiency calculated at 100 m. Export efficiency ranged between 6-7% of the NPP (from satellite data estimates) exiting the 0-100 m layer. The attenuation rate of carbon flux was determined using a power law regression fit. The  $b$  values ranged between - 0.4 and - 0.6. The

Deleted: <sup>3</sup>

Deleted: <sup>3</sup>

Deleted:

Deleted: <sup>3</sup>

Formatted: English (UK)

337 ~~highest~~ transfer efficiency was found during event 2, where 40% of the flux at 100m reaches 1000m, followed by  
338 the between-outside mask and event 1 (31% and 29%, respectively; Table 1).

339 **Table 1: Parameters characterizing the biological carbon pump efficiency calculated in the plumes**

	Outside-between mask	event 1	event 2
E <sub>eff</sub>	7%	7%	6%
T <sub>eff</sub>	31%	29%	40%
b	-0.48	-0.53	-0.6

340 **3.4 Particle composition**

341 **3.4.1 Morphotypes of marine snow and composition of the different events**

342 The k-means clustering applied to the PCA coordinates helped us to distinguish between five marine snow  
343 morphotypes illustrated in Figure 5. Type 1 consisted of ~~large, compact objects with an Equivalent Spherical~~  
344 ~~Diameter (ESD)>0.8mm referred to as~~ big and dense objects (Big Dense Particles, BDP) with an Equivalent  
345 Spherical Diameter (ESD)>0.8mm. Type 2 comprised elongated, ~~thread-like~~ objects ~~termed~~ Fiber particles, (FP),  
346 and type 3 consisted of ~~large, bright, and porous objects referred to as~~ Big Porous particles, (BPP). Type 4 was  
347 mainly formed of dense, small, and circular objects (Small Dense particles: SDP) and type 5 consisted of ~~small,~~  
348 ~~bright~~ and porous objects ~~Small Porous particles, (SPP)~~. These five morphotypes were then used to characterize the  
349 distribution and composition of marine snow. It should be noted that the terms "porous" and "dense" refer to  
350 brightness, with "porous" indicating greater light transmission, ~~while "dense" denotes lower light transmission.~~

Deleted: best

Formatted Table

Deleted: (

Deleted: :

Deleted: big

Deleted: (

Deleted: :

Deleted: light grey,

Deleted: (

Deleted: :

Deleted: .

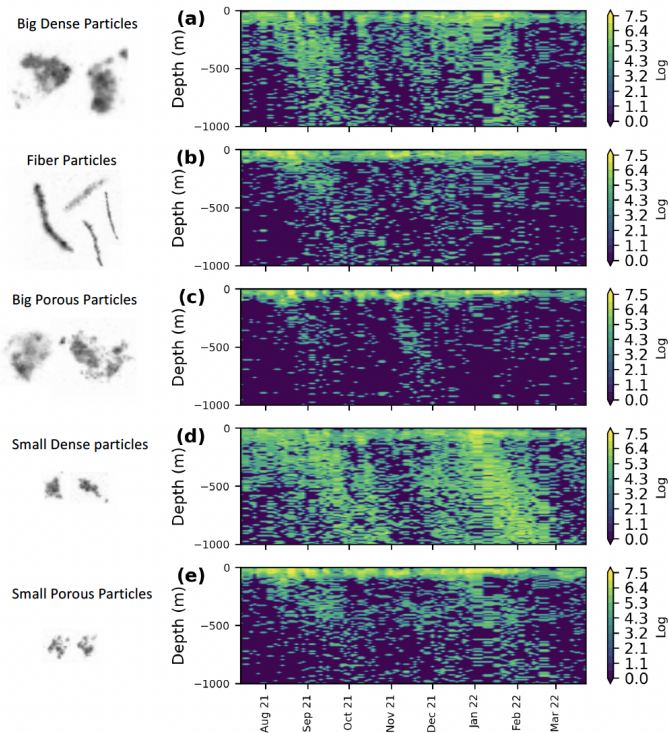


**Figure 5: Time series of the logarithmic concentration of (a) Big Dense, (b) Fiber, (c) Big Porous, (d) Small Dense, and (e) Small Porous morphotypes.**

The different detritus morphotypes showed high concentrations of particles in the surface, especially during the export events (Fig. 5, S7). They shared similar temporal dynamics primarily in the surface layer: FP, BPP, BDP, SDP, and SPP decreased exponentially between 0 and 150 m. While FB, BPP and SPP decreased slowly throughout the water column in the mesopelagic layers, BDP and SDP increased gradually between 400-600 m and then decreased again (Fig. S7). BDP and SDP presented two discernable plumes during the two delineated export events, reaching 2000 m with significant concentrations all along the plumes (Fig. 6a,d, S6). Other morphotypes such as FP and SPP were sometimes present in deeper layers but with low concentrations. In the deeper mesopelagic, only SDP showed no decrease with depth (Fig. S7).

SPP were most abundant across the different periods (Fig. S7). For the outside-between mask, these particles constituted 28% within the 0-100 m range. In events 1 and 2, their presence increased up to 50-60% within the 0-50 m range (Fig. S7). However, this percentage notably declined between 50-100 m for events 1 and 2 with values dropping to 25% below 100 m. It further decreased between 100-150 m outside of these events, 18% below 150 m (Fig. S7). BPP and FP also exhibited high concentrations within the upper 100 m where they were primarily located.

Even though BDP and SDP were the least preponderant classes in the first 100 m, they dominated deeper layers compared to clusters BPP, SPP, and FP which were found almost exclusively in the surface layer. Their proportions were more than 20% for events 1 and 2 and 15% outside of these export events in the first 100 m. Concentrations of small, dark, and compact marine snow decreased until 200 m and then increased until 1000 m, while big, dark, and compact particles decreased until 400–450 m for all masks and increased afterward (Fig. S7). Small compact particles showed a mean proportion of more than 40% for both events and 28% for the period outside of those (Fig S7). Throughout the observation period, the vertical attenuation of dark, compact, and small particles was the lowest of all marine snow categories with visibly more dark dense morphotypes in deep waters for all periods, while the highest vertical attenuation amongst all marine snow types was observed for the BPP cluster.

### 3.5 Lagrangian diagnostics

To determine the optimal advective time scale for the different particle sizes, we correlated both MiP and MaP abundance in the first 100 m with the Lagrangian chl-a (chlorophyll in the moving water mass) for the different advective times (from 0–45 days). The highest correlation was determined for  $t=15$  days (Fig. S8). Chl-a and BBP POC were positively correlated with MiP in the first 100 m (Fig. S9). While MaP showed a low correlation with chl-a. As for the different morphotypes, FP, SDP, and SPP were significantly correlated with chl-a while no significant correlation was observed with BDP and BPP. POC flux, MiP, and MaP abundances were also significantly correlated with the Lagrangian vorticity and divergence for an advective time scale of 15 days.

## 4. Discussion

### 4.1 Cold tongue and TIW related equatorial upwelling dynamics

The equatorial Atlantic follows a pronounced seasonal cycle in upwelling activity, forced by the seasonal winds and the meridional migration of the intertropical convergence zone (Brandt et al., 2023), which translates into a respective cycle of productivity (Grodsky et al. 2008) and a slight seasonality in carbon export (Fischer et al., 2000; Wefer & Fischer, 1993).

Here, we use a combination of satellite data analysis and in situ biogeochemical and image-based measurements from a BGC-Argo / UVP float to further our understanding of equatorial Atlantic biological pump dynamics. We observed relatively cool SST between August and October corresponding to the occurrence of the Atlantic Cold Tongue (ACT; Brandt et al., 2011), and during boreal winter in December and February corresponding to a secondary cooling period as was reported by Jouanno et al. (2011) and Okumura & Xie (2006). Seasonal cooling events are largely linked to diapycnal heat flux out of the mixed layer into the deeper ocean (Hummels et al., 2013). This heat flux is due to the enhancement of the vertical shear driven by the strength and the direction of the surface current (Jouanno et al., 2011) and the eastward Equatorial Undercurrent (EUC) at the thermocline level (Hummels et al., 2013). The equatorial Atlantic was warmer than usual at the surface throughout the boreal summer of 2021. This was the result of the occurrence of a strong Atlantic Niño driven by wind and equatorial wave forcings (Lee et al., 2023; Song et al., 2023; Tuchen et al., 2024). The physical processes controlling the downward heat flux out of the mixed layer also control the upward supply of nitrate to the euphotic layer (Radenac et al., 2020). The equatorial Atlantic is a nitrate-limited upwelling regime (Grodsky et al., 2008; Moore et al., 2013) and modeling studies showed that in the equatorial Atlantic, the seasonal variations in chl-a are closely linked to the seasonal variability of the nitrate input via upwelling and mixing (Loukos & Mémery, 1999; Radenac et al., 2020). The chl-

a blooms that are normally found in the equatorial Atlantic are linked to the upwelling of nitrate-rich thermocline waters during these periods and the diffusive flux of nitrate into the mixed layer through mixing (Longhurst, 1993; Radenac et al., 2020). Likewise, we found that chl-a concentration followed a pronounced semiannual cycle with peaks in boreal summer and winter, as also described by Grodsky et al. (2008) and Brandt et al. (2023). During the first peak, from August to October, the thermocline was relatively deep compared to climatology (as a consequence of the presence of the Atlantic Niño), and chl-a levels were likewise relatively low. A shallower nitracline together with a shallower EUC (Tuchen et al., 2024) during the second peak in boreal winter might have favored the growth of the phytoplankton assemblage showing anomalously high chl-a levels. These variations with respect to the climatological cycle are in agreement with what was proposed by Grodsky et al. (2008) that the interannual variability of the secondary bloom in boreal winter is as large as those of the primary bloom in boreal summer, even though its climatological expression is weaker.

Another process affecting local productivity at the equator is intraseasonal TIWs with a 20-50 days period range as indicated by the bandpass-filtered SST and chl-a anomalies. In this study, elevated primary production was located between 10°W-25°W in a region affected by TIWs. Their occurrence strongly suggests that TIWs might influence the biogeochemistry of the equatorial upper-ocean system. On the one hand, TIWs are associated with meridional currents at the equator modulating the boundary of the Atlantic cold tongue eventually resulting in local variations of SST and chl-a. On the other hand, TIWs are associated with phases of enhanced mixing (Foltz et al., 2020; Heukamp et al., 2022; Inoue et al., 2019; Moum et al., 2009) or front generation (Warner et al., 2018) leading to upward nutrient supply. It has been suggested that TIWs could enhance upper-ocean fertilization by promoting local nitrate upwelling alleviating the nitrate depletion which usually affects this region (Radenac et al., 2020; Sherman et al., 2022). Enhanced chlorophyll concentration has been associated with TIWs suggesting that TIWs drive intraseasonal chl-a variability (Grodsky et al., 2008; Menkes et al., 2002; Shi & Wang, 2021). Pronounced positive and negative anomalies in bandpass-filtered chl-a data were anti-correlated with anomalies in bandpass-filtered positive SST anomalies. The SST anomalies were moderate during the secondary bloom in boreal winter, accompanied by a shallower thermocline. However, during that period, a pronounced chl-a bloom was observed together with the largest bandpass-filtered chl-a anomalies.

In brief, the development of the cold tongue during boreal summer, the secondary cooling during boreal winter, and the presence of TIWs in the equatorial Atlantic exert major controls on the surface ocean hydrographic characteristics and biogeochemistry on intraseasonal to seasonal time scales. We suggest that the combination of seasonal thermocline upwelling and TIWs was responsible for the observed enhanced chl-a signals indicating enhanced variability of primary productivity. Therefore, we can examine their impact on particulate matter build up and export.

#### 4.2 Upwelling events translate into size-differentiated enhanced export from the mixed layer

The timing of the two upwelling events which lead to chl-a accumulation is consistent with the objective detection of two peaks in the MaP concentration. Both MiP and MaP in top 100 m are correlated to the in situ chl-a biomass suggesting that the primary producers provided the elemental particles for the two size classes of marine snow aggregates. Stronger correlation with MiP than with MaP may indicate that MaP are formed with a delay through the transformation of MiP by aggregation. This is also supported by Lagrangian chl-a which is more correlated

453 with MiP and MaP (for the same advective time scale of 10 to 15 days) than with concomitant in situ chl-a biomass.  
454 This time scale is consistent with particle aggregation by coagulation of phytoplankton cells followed by the export  
455 of aggregates (Burd & Jackson, 2009; Jackson, 1990). Correlation between Lagrangian chl-a and MiP emphasizes  
456 that MiP are also built up with time.

457 More comprehensive understanding of pelagic functioning can arise from the identification of marine snow  
458 morphotypes (Trudnowska et al., 2021). Fiber Particles (FP), Small Dense particles (SDP), and Small Porous  
459 Particles (SPP) in the epipelagial were significantly correlated with chl-a while no significant correlation was  
460 observed for BDP and BPP. This means that both fiber and porous aggregates might be of phytoplanktonic origin.  
461 Elongated or porous particles in the surface layer, for example, can result from phytoplankton colonies such as  
462 diatom chains or *Trichodesmium* colonies (Dupouy et al., 2018; Villareal et al., 2011) (Fig. S10). These diatoms  
463 were mostly detected during event 1 in our study, their presence increases in conditions of high export systems  
464 (Henson et al., 2019). Porous aggregates might be associated with the accumulation of phytoplankton biomass.  
465 When the bloom is massive enough to enhance aggregation, small porous aggregates are precursors of bigger ones.  
466 As for dense particles, they could be potential fecal pellets produced by zooplankton's feeding as generally found  
467 in other studies (Stemmann & Boss, 2012; Trudnowska et al., 2021), but they could also originate from other  
468 sources such as aggregated phytoplankton or phytodetritus (Alldrege & Silver, 1988; Guidi et al., 2009).

Deleted: .

469 All morphotypes, particle size classes and POC flux were significantly correlated with Lagrangian vorticity and  
470 divergence highlighting that physical dynamics of the upper ocean (such as up- and downwelling) leading to  
471 primary production were the primary control in particle production and transformations. In their paper, Siegel et  
472 al. (2024) found that turbulence levels close to the surface tend to favor smaller particle sizes and increase  
473 fragmentation while turbulence near the base of the mixed layer encourages coagulation and the formation of larger  
474 particles.

475 POC production is associated with phytoplankton production which ultimately influences the export flux. To  
476 investigate the ratio of POC flux leaving the euphotic zone, we calculated the export efficiency ratio at 100 m  
477 during and outside of the events. The export efficiency (e-ratio) was 6-7% and fell within the global average e-ratio  
478 range (Bam et al., 2023 and references within). These values suggest that strong remineralization occurs in surface  
479 waters, aligning with existing literature (Clements et al., 2022). The same e-ratio during and outside of events  
480 highlights the stability of the export efficiency of the equatorial system. One of the hypotheses explaining this  
481 stability is the distribution and contribution of the morphotypes during and outside of export events. During and  
482 before export events, all five morphotypes were detected, with proportions varying with depth. This suggests that  
483 within our observation period, the equatorial region, during or before export events, possesses a similar  
484 phytoplanktonic bloom behavior leading to the same marine snow morphotypes which might explain the similar  
485 behavior of the biological pump. This is in contrast with what was observed for the Arctic system, where two  
486 successive blooms of different nature occur and are associated with different morphotypes. The first bloom was an  
487 ice edge bloom and was dominated by diatoms, while the second was ice free and was associated with the presence  
488 of *Phaeocystis* leading to agglomerated morphotypes and their slow settling compared to the first bloom  
489 (Trudnowska et al., 2021). These differences in morphotypes reflect not only contrasting environmental conditions  
490 between the Arctic and equatorial Atlantic, but also distinct bloom successions and morpho dynamic responses.



supporting the idea that regional ecosystem characteristics shape marine snow structure and its role in export processes.

Another hypothesis for the stability of the system might be related to the tight coupling between primary production and export. In this study, the lag between PP and particle production was estimated to be 10-15 days, corresponding to a similarly short lag determined by Henson et al. (2015) usually found in upwelling regions. This lag increases with the increase of seasonality and also affects the seasonality of the  $e_{\text{eff}}$  (Henson et al., 2015). In our case, the same  $e_{\text{eff}}$  highlights the low seasonality of the carbon pump in the equatorial system: producers and grazers are tightly coupled due to the low seasonality in PP and export (Owens et al., 2015). This coupling might be due to the combination of euphotic-zone irradiance and the supply of nutrients: strong light penetration combined with the energetic intraseasonal variability of the system bringing nutrients to the surface (Menkes et al., 2002), allows producers to be present all year long in the surface layer. Further studies on the dynamics and composition of detrital particles in bloom situations, in combination with planktonic measurements, are necessary to understand surface dynamics of particle formation and export.

#### 4.3 Deep particle sequestration is driven by compact particles

Particle production within the upper 100 m led to the formation of sinking plumes reaching down to 2000 m of depth. Although particle concentrations were higher during export events, the vertical carbon flux, within and outside the plumes followed the general asymptotic shape characteristic of particle flux observations, with rapid attenuation in the surface layer transitioning to a more gradual decrease in the bathypelagic layer. This was also true for the MiP and MaP abundances. More likely, the observed general decrease in small and big particles is driven by biological processes such as degradation and aggregation. Yool et al. (2013), using a biogeochemical model, attributed the flux of particles at deep depths of the ocean to MaPs. However, Kiko et al. (2017) found an abundance of MiPs in the bathypelagic zone that can be observed down to the sea floor. They suggest that shedding and other disaggregation processes might result in a more effective export of particulate matter, both actively and passively. We suggest that their presence in the meso- and bathypelagic layer highlights both their important roles in contributing to the flux. The difference in flux amplitude inside versus outside of the plumes, along with the higher particle concentration within the plumes, suggests a seasonal pulse in flux to the deep sea, as previously described by Beaulieu (2002). This rapid and deep flux is mainly associated with bloom events, consistent with earlier observations of flux events (flux at 3000 m,  $2.07 \text{ mg C m}^{-2} \text{ d}^{-1}$ ), reaching depths of up to 4000 m (Beaulieu, 2002; Kiko et al., 2017; Lampitt et al., 1993).

We combined the quantitative analysis of particle mass distribution with particle image analysis to investigate the nature of particles exported to deeper layers. In this study, SDP were more deeply exported compared to other morphotypes, indicating that most of the MaP abundance found at depth is dominated by small dense particles. This trend toward more circular and less elongated aggregates with increasing depth confirms prior research (Drago, 2023; Trudnowska et al., 2021; Accardo et al., submitted). SDP vertical profiles also showed a particle maximum between 450 and 800 m as found by Kiko et al. (2017) and Siegel et al. (2024), unlike the rest of the morphotypes which attenuated with depth. The observed increase in small particles is more likely driven by diel vertical migrations of zooplankton that actively exports organic material to depth (Hidaka et al., 2001; Turner, 2015). Most of the float profiles were conducted during the night (approximately 50%), which further supports the

Formatted: English (UK)

interpretation that the increased abundance of small dense particles at depth is linked to nocturnal zooplankton migration. This can be confirmed by the increase of zooplankton for all periods between 300-600 m (Fig. S11) coinciding with the depth of increase of dense particles and the upper limit of zooplankton migration depth extracted from shipboard ADCP data (shown in Fig. S11) and the range mentioned in Kiko et al., (2017) and Bianchi & Mislan, (2016). Kiko et al. (2017) also found a particle maximum between 300 and 600 m in the equatorial Atlantic and attributed it to migrating zooplankton. Food ingested near the surface is carried downward in the guts of migrating zooplankton to be egested, eaten by consumers of zooplankton, or metabolized at depth (Packard & Gómez, 2013). Model studies suggest that zooplankton diel vertical migration might account for 10-30% of the total vertical flux of carbon downward from epipelagic layers (Bianchi et al., 2013), enhancing the efficiency of carbon export (Gorgues et al., 2019) through the generation of fecal pellets which can be incorporated in marine snow. Kiko et al. (2020) found that gut flux and mortality might make up about 30-40% of particulate matter supply to the 300-600 m depth layer in the eastern tropical North Atlantic and that the amount of carbon supplied via these mechanisms could suffice to generate a flux and particle increase.

Because our study includes periods of both high and low export, we aimed to assess the flux attenuation rate by calculating the transfer efficiency for different periods. The transfer efficiency was estimated using flux at depths of 100 m and 1000 m. Although our export reached depths of 2000 m, we selected the 1000 m layer due to the relatively small reduction in POC flux with increasing depth, as noted by Francois et al. (2002).  $T_{eff}$  values obtained in our study indicate a high efficiency of the biological pump with up to 40% of the organic material exported at 100 m also reaching 1000 m, regardless of the conditions. This means that despite seasonal variation in primary production and carbon flux during and outside of export events, the biological pump exhibits a consistent response in the equatorial region, rendering it a predictable system. The  $b$  values calculated (around 0.5) show a low attenuation rate of the computed POC flux, suggesting that part of the particulate matter exported at the equator and undergoes little further remineralization at mesopelagic depths (Henson et al., 2015; Omand et al., 2015). Global studies showcased the seasonal and regional variability in the exponent  $b$  and showed values around 0.7 in Guidi et al, (2015) and 0.6 in Henson et al., (2012) for the tropical equatorial region. The consistent low  $e$ -ratio associated with high  $T_{eff}$  aligns with the pattern proposed by Guidi et al, (2015) and Henson et al., (2012). This means that deeper particle injection and rapid sinking result in longer carbon sequestration as the time a given water parcel needs to travel from the ocean interior to the surface increases with depth.

For the first time, we characterized the distribution of particles within an export plume, and offered a morphological description of exported particles using in situ imaging. The comparisons made with previous studies for the  $e$ -ratio and the transfer efficiency show that opting for the plume method yields more accurate results and a more comprehensive understanding of the fate of particles along their progression into deeper layers (Table S1).

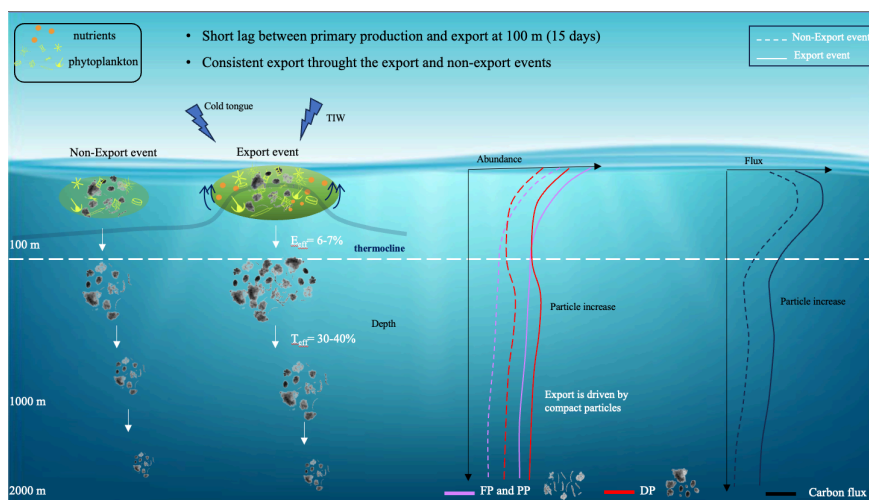


**Figure 6: Illustrative example of the particle export system in the Atlantic equatorial region during export and non-export events. FP: fiber particles, PP: porous particles, DP: dense particles. Teff: Transfer efficiency, Eeff: Export efficiency, TIW: Tropical instability Wave. We do not distinguish between small and large particles, as the particle composition remains consistent across both export and non-export events and only the concentration changes.**

## 5 Conclusion

The integration of the UVP on an Argo float has allowed us to study the temporal variability and the dynamics of the BCP. Our study follows the particle dynamics along the water column in the equatorial Atlantic region between July 2021 and March 2022 including the strong 2021 Atlantic Niño event, using the plume method and a novel BGC-Argo/UVP6 dataset. Ocean dynamics in the equatorial system exhibit a seasonal cycle with a decrease in temperature during boreal summer and winter leading to the presence of two distinct blooms. These blooms are characterized by significant export events reaching depths of 2000 m. The production and export of carbon during that year was dampened because of the strong Atlantic Niño event during boreal summer 2021. Detritus were classified into five distinct morphotypes based on morphological variables. In surface waters, marine snow is dominated by porous aggregates and fibers while deeper layers primarily receive big and small dense particles during export events. Unlike most of the morphotypes decreasing with depth, dense particles show an increase between 300-600 m. Zooplankton diel vertical migration might play a role in the generation of a particle maximum at intermediate layers consisting of the small dense cluster. The equatorial region acts as a stable export system throughout all periods observed, with an export efficiency steadily ranging between 6-7% probably due to the short lag between the primary production and the export and the same morphotype composition along the year. Regardless of the initial conditions, 30-40% of the flux at 100 m is exported to 1000 m. Such consistency highlights the equilibrium inherent in the equatorial region's carbon dynamics along the float trajectory during this special event, providing further context to the observed patterns of carbon and particle export. Moreover, it underscores the necessity for additional observations to ascertain whether the system is truly stable over the long term. This study contributes to a deeper understanding of the intricacies of carbon cycling in equatorial waters using autonomous vehicle-derived estimates of particle fluxes. By elucidating the role of export events and different particle morphotypes, we underscore the significance of these factors in shaping the equatorial biological pump.

Formatted

589 The successful combination of the UVP6 with other float sensors and the development of a continuous monitoring  
590 strategy will provide insights that were previously unattainable with sparse and temporally limited shipboard and  
591 moored sediment trap observations.

## 592 6 Code availability

593 The codes used post-data treatment are available ~~on this GitHub repository:~~  
594 <https://github.com/joellehabib/Floatpaper.git>.

Deleted: upon request to the lead author

## 595 7 Data availability

596 The sea surface temperature data is available on the NOAA website at:  
597 <https://psl.noaa.gov/data/gridded/data.noaa.oisst.v2.highres.htm>. Float data are available at <https://argo.ucsd.edu>.  
598 Data used in this manuscript for the carbon flux and particle concentrations are available online using the following  
599 DOI: 10.5281/zenodo.14007570. Further data can be made available by the authors upon request.

## 600 8 Author contribution

601 JH, RK, and LS developed the study's concept. RK, LS, JH, FPT, PB, and AB contributed to data acquisition; RK,  
602 LS, JH, PB, AA, AB, and FPT contributed substantially to the data analysis; JH wrote the initial version of the  
603 paper. All authors contributed substantially to drafting the manuscript; All authors approved the final submitted  
604 manuscript.

## 605 9 Competing interests

606 The authors declare that they have no conflict of interest.

## 607 9 Acknowledgments

608 The study was supported by EU H2020 under grant agreement 817578 TRIATLAS project. RK acknowledges  
609 support via a Make Our Planet Great Again grant from the French National Research Agency (ANR) within the  
610 Programme d'Investissements d'Avenir #ANR-19-MPGA-0012 and funding from the Heisenberg Programme of  
611 the German Science Foundation #KI 1387/5-1. We thank the crews, scientists, and technicians involved in the  
612 deployment and recovery of the Argo float during RV *Sonne* cruise SO284 and PIRATA FR32 cruise with RV  
613 *Thalassa*.

## 614 10 References

615 Alldredge, A. L. and Silver, M. W.: Characteristics, dynamics and significance of marine snow, Prog. Oceanogr.,  
616 20, 41–82, [https://doi.org/10.1016/0079-6611\(88\)90053-5](https://doi.org/10.1016/0079-6611(88)90053-5), 1988.  
617 [Armstrong, R. A., Lee, C., Hedges, J. I., Honjo, S., and Wakeham, S. G.: A new, mechanistic model for organic](#)  
618 [carbon fluxes in the ocean based on the quantitative association of POC with ballast minerals, Deep Sea Res. Part](#)  
619 [II Top. Stud. Oceanogr., 49, 219–236, https://doi.org/10.1016/S0967-0645\(01\)00101-1, 2002.](#)  
620 Athie, G. and Marin, F.: Cross-equatorial structure and temporal modulation of intraseasonal variability at the  
621 surface of the Tropical Atlantic Ocean, J. Geophys. Res., 113, C08020, <https://doi.org/10.1029/2007JC004332>,  
622 2008.

Formatted: Font colour: Auto, English (UK)

624 Bach, L. T., Stange, P., Taucher, J., Achterberg, E. P., Algueró-Muñiz, M., Horn, H., Esposito, M., and Riebesell,  
 625 U.: The Influence of Plankton Community Structure on Sinking Velocity and Remineralization Rate of Marine  
 626 Aggregates, *Glob. Biogeochem. Cycles*, 33, 971–994, <https://doi.org/10.1029/2019GB006256>, 2019.  
 627 Bam, W., Gasser, B., Maiti, K., Levy, I., Miquel, J. C., Hansman, R. L., Scholten, J., Xie, R. C., Sommer, S., Kiko,  
 628 R., and Swarzenski, P. W.: Particulate organic carbon export fluxes estimates by  $^{234}\text{Th}/^{238}\text{U}$  disequilibrium in the  
 629 oxygen minimum zone off the Peruvian coast, *Mar. Chem.*, 257, 104325, <https://doi.org/10.1016/j.marchem.2023.104325>, 2023.  
 630 Baudena, A., Ser-Giacomi, E., D’Onofrio, D., Capet, X., Cotté, C., Cherel, Y., and D’Ovidio, F.: Fine-scale  
 631 structures as spots of increased fish concentration in the open ocean, *Sci. Rep.*, 11, 15805,  
 632 <https://doi.org/10.1038/s41598-021-94368-1>, 2021.  
 633 Beaulieu, S. E.: Accumulation and fate of phytodetritus on the sea floor, 2002.  
 634 Bernardello, R., Marinov, I., Palter, J. B., Sarmiento, J. L., Galbraith, E. D., and Slater, R. D.: Response of the  
 635 Ocean Natural Carbon Storage to Projected Twenty-First-Century Climate Change, *J. Clim.*, 27, 2033–2053,  
 636 <https://doi.org/10.1175/JCLI-D-13-00343.1>, 2014.  
 637 Bianchi, D. and Mislan, K. a. S.: Global patterns of diel vertical migration times and velocities from acoustic data,  
 638 *Limnol. Oceanogr.*, 61, 353–364, <https://doi.org/10.1002/lno.10219>, 2016.  
 639 Bianchi, D., Galbraith, E. D., Carozza, D. A., Mislan, K. A. S., and Stock, C. A.: Intensification of open-ocean  
 640 oxygen depletion by vertically migrating animals, *Nat. Geosci.*, 6, 545–548, <https://doi.org/10.1038/ngeo1837>,  
 641 2013.  
 642 Bianchi, D., Weber, T. S., Kiko, R., and Deutsch, C.: Global niche of marine anaerobic metabolisms expanded by  
 643 particle microenvironments, *Nat. Geosci.*, 11, 263–268, <https://doi.org/10.1038/s41561-018-0081-0>, 2018.  
 644 Biddanda, B. and Pomeroy, L.: Microbial aggregation and degradation of phytoplankton-derived detritus in  
 645 seawater. I. Microbial succession, *Mar. Ecol. Prog. Ser.*, 42, 79–88, <https://doi.org/10.3354/meps042079>, 1988.  
 646 Bopp, L., Resplandy, L., Orr, J. C., Doney, S. C., Dunne, J. P., Gehlen, M., Halloran, P., Heinze, C., Ilyina, T.,  
 647 Séférian, R., Tjiputra, J., and Vichi, M.: Multiple stressors of ocean ecosystems in the 21st century: projections  
 648 with CMIP5 models, *Biogeosciences*, 10, 6225–6245, <https://doi.org/10.5194/bg-10-6225-2013>, 2013.  
 649 Boyd, P. W., Claustre, H., Levy, M., Siegel, D. A., and Weber, T.: Multi-faceted particle pumps drive carbon  
 650 sequestration in the ocean, *Nature*, 568, 327–335, <https://doi.org/10.1038/s41586-019-1098-2>, 2019.  
 651 Brandt, P., Caniaux, G., Bourlès, B., Lazar, A., Dengler, M., Funk, A., Hormann, V., Giordani, H., and Marin, F.:  
 652 Equatorial upper-ocean dynamics and their interaction with the West African monsoon, *Atmospheric Sci. Lett.*, 12,  
 653 24–30, <https://doi.org/10.1002/asl.287>, 2011.  
 654 Brandt, P., Alory, G., Awo, F. M., Dengler, M., Djakouré, S., Imbol Koungue, R. A., Jouanno, J., Körner, M.,  
 655 Roch, M., and Rouault, M.: Physical processes and biological productivity in the upwelling regions of the tropical  
 656 Atlantic, *Ocean Sci.*, 19, 581–601, <https://doi.org/10.5194/os-19-581-2023>, 2023.  
 657 Briggs, N., Perry, M. J., Cetinić, I., Lee, C., D’Asaro, E., Gray, A. M., and Rehm, E.: High-resolution observations  
 658 of aggregate flux during a sub-polar North Atlantic spring bloom, *Deep Sea Res. Part Oceanogr. Res. Pap.*, 58,  
 659 1031–1039, <https://doi.org/10.1016/j.dsr.2011.07.007>, 2011.  
 660 Briggs, N., Dall’Olmo, G., and Claustre, H.: Major role of particle fragmentation in regulating biological  
 661 sequestration of  $\text{CO}_2$  by the oceans, *Science*, 367, 791–793, <https://doi.org/10.1126/science.aay1790>, 2020.  
 662 Buesseler, K. O., Lamborg, C. H., Boyd, P. W., Lam, P. J., Trull, T. W., Bidigare, R. R., Bishop, J. K. B., Casciotti,

664 K. L., Dehairs, F., Elskens, M., Honda, M., Karl, D. M., Siegel, D. A., Silver, M. W., Steinberg, D. K., Valdes, J.,  
665 Van Mooy, B., and Wilson, S.: Revisiting Carbon Flux Through the Ocean's Twilight Zone, *Science*, 316, 567–  
666 570, <https://doi.org/10.1126/science.1137959>, 2007.

667 Buesseler, K. O., Boyd, P. W., Black, E. E., and Siegel, D. A.: Metrics that matter for assessing the ocean biological  
668 carbon pump, *Proc. Natl. Acad. Sci.*, 117, 9679–9687, <https://doi.org/10.1073/pnas.1918114117>, 2020.

669 Burd, A. B. and Jackson, G. A.: Particle Aggregation, *Annu. Rev. Mar. Sci.*, 1, 65–90,  
670 <https://doi.org/10.1146/annurev.marine.010908.163904>, 2009.

671 Cael, B. B., Cavan, E. L., and Britten, G. L.: Reconciling the Size-Dependence of Marine Particle Sinking Speed,  
672 *Geophys. Res. Lett.*, 48, e2020GL091771, <https://doi.org/10.1029/2020GL091771>, 2021.

673 Claustre, H., Johnson, K. S., and Takeshita, Y.: Observing the Global Ocean with Biogeochemical-Argo, *Annu.*  
674 *Rev. Mar. Sci.*, 12, 23–48, <https://doi.org/10.1146/annurev-marine-010419-010956>, 2020.

675 Clements, D. J., Yang, S., Weber, T., McDonnell, A. M. P., Kiko, R., Stemmann, L., and Bianchi, D.: Constraining  
676 the Particle Size Distribution of Large Marine Particles in the Global Ocean With *In Situ* Optical Observations and  
677 Supervised Learning, *Glob. Biogeochem. Cycles*, 36, e2021GB007276, <https://doi.org/10.1029/2021GB007276>,  
678 2022.

679 Clements, D. J., Yang, S., Weber, T., McDonnell, A. M. P., Kiko, R., Stemmann, L., and Bianchi, D.: New Estimate  
680 of Organic Carbon Export From Optical Measurements Reveals the Role of Particle Size Distribution and Export  
681 Horizon, *Glob. Biogeochem. Cycles*, 37, e2022GB007633, <https://doi.org/10.1029/2022GB007633>, 2023.

682 De Boyer Montégut, C., Madec, G., Fischer, A. S., Lazar, A., and Iudicone, D.: Mixed layer depth over the global  
683 ocean: An examination of profile data and a profile-based climatology, *J. Geophys. Res. Oceans*, 109,  
684 2004JC002378, <https://doi.org/10.1029/2004JC002378>, 2004.

685 De La Rocha, C. L.: The biological pump, Elsevier, Amsterdam Heidelberg, 2004.

686 DeVries, T., Primeau, F., and Deutsch, C.: The sequestration efficiency of the biological pump, *Geophys. Res.*  
687 *Lett.*, 39, 2012GL051963, <https://doi.org/10.1029/2012GL051963>, 2012.

688 Dilling, L. and Alldredge, A. L.: Fragmentation of marine snow by swimming macrozooplankton: A new process  
689 impacting carbon cycling in the sea, *Deep Sea Res. Part Oceanogr. Res. Pap.*, 47, 1227–1245,  
690 [https://doi.org/10.1016/S0967-0637\(99\)00105-3](https://doi.org/10.1016/S0967-0637(99)00105-3), 2000.

691 Dupouy, C., Frouin, R., Tedetti, M., Maillard, M., Rodier, M., Lombard, F., Guidi, L., Picheral, M., Neveux, J.,  
692 Duhamel, S., Charrière, B., and Sempéré, R.: Diazotrophic Trichodesmium impact on UV–Vis radiance and  
693 pigment composition in the western tropical South Pacific, *Biogeosciences*, 15, 5249–5269,  
694 <https://doi.org/10.5194/bg-15-5249-2018>, 2018.

695 Engel, A., Cisternas-Novoa, C., Hauss, H., Kiko, R., and Le Moigne, F. A. C.: Hypoxia-tolerant zooplankton may  
696 reduce biological carbon pump efficiency in the Humboldt current system off Peru, *Commun. Earth Environ.*, 4,  
697 458, <https://doi.org/10.1038/s43247-023-01140-6>, 2023.

698 Fabri-Ruiz, S., Baudena, A., Moullec, F., Lombard, F., Irisson, J.-O., and Pedrotti, M. L.: Mistaking plastic for  
699 zooplankton: Risk assessment of plastic ingestion in the Mediterranean sea, *Sci. Total Environ.*, 856, 159011,  
700 <https://doi.org/10.1016/j.scitotenv.2022.159011>, 2023.

701 Fischer, G., Ratmeyer, V., and Wefer, G.: Organic carbon fluxes in the Atlantic and the Southern Ocean:  
702 relationship to primary production compiled from satellite radiometer data, 2000.

703 Foltz, G. R., Hummels, R., Dengler, M., Perez, R. C., and Araujo, M.: Vertical Turbulent Cooling of the Mixed

704 Layer in the Atlantic ITCZ and Trade Wind Regions, *J. Geophys. Res. Oceans*, 125, e2019JC015529,  
 705 <https://doi.org/10.1029/2019JC015529>, 2020.  
 706 Forest, A., Babin, M., Stemann, L., Picheral, M., Sampei, M., Fortier, L., Gratton, Y., Bélanger, S., Devred, E.,  
 707 Sahlin, J., Doxaran, D., Joux, F., Ortega-Retuerta, E., Martín, J., Jeffrey, W. H., Gasser, B., and Carlos Miquel, J.:  
 708 Ecosystem function and particle flux dynamics across the Mackenzie Shelf (Beaufort Sea, Arctic Ocean): an  
 709 integrative analysis of spatial variability and biophysical forcings, *Biogeosciences*, 10, 2833–2866,  
 710 <https://doi.org/10.5194/bg-10-2833-2013>, 2013.  
 711 Fox, J. E., Behrenfeld, M., Halsey, K. H., and Graff, J.: Global estimates of particulate organic carbon from the  
 712 surface ocean to the base of the mesopelagic, <https://doi.org/10.22541/essoar.171017314.40658424/v1>, 11 March  
 713 2024.  
 714 Giering, S. L. C., Sanders, R., Lampitt, R. S., Anderson, T. R., Tamburini, C., Boutrif, M., Zubkov, M. V., Marsay,  
 715 C. M., Henson, S. A., Saw, K., Cook, K., and Mayor, D. J.: Reconciliation of the carbon budget in the ocean's  
 716 twilight zone, *Nature*, 507, 480–483, <https://doi.org/10.1038/nature13123>, 2014.  
 717 Gorgues, T., Aumont, O., and Memery, L.: Simulated Changes in the Particulate Carbon Export Efficiency due to  
 718 Diel Vertical Migration of Zooplankton in the North Atlantic, *Geophys. Res. Lett.*, 46, 5387–5395,  
 719 <https://doi.org/10.1029/2018GL081748>, 2019.  
 720 Grodsky, S. A., Carton, J. A., and McClain, C. R.: Variability of upwelling and chlorophyll in the equatorial  
 721 Atlantic, *Geophys. Res. Lett.*, 35, L03610, <https://doi.org/10.1029/2007GL032466>, 2008.  
 722 Guidi, L., Jackson, G. A., Stemann, L., Miquel, J. C., Picheral, M., and Gorsky, G.: Relationship between particle  
 723 size distribution and flux in the mesopelagic zone, *Deep Sea Res. Part Oceanogr. Res. Pap.*, 55, 1364–1374,  
 724 <https://doi.org/10.1016/j.dsr.2008.05.014>, 2008.  
 725 Guidi, L., Stemann, L., Jackson, G. A., Ibanez, F., Claustre, H., Legendre, L., Picheral, M., and Gorsky, G.:  
 726 Effects of phytoplankton community on production, size, and export of large aggregates: A world-ocean analysis,  
 727 *Limnol. Oceanogr.*, 54, 1951–1963, <https://doi.org/10.4319/lo.2009.54.6.1951>, 2009.  
 728 Guidi, L., Legendre, L., Reygondeau, G., Uitz, J., Stemann, L., and Henson, S. A.: A new look at ocean carbon  
 729 remineralization for estimating deepwater sequestration, *Glob. Biogeochem. Cycles*, 29, 1044–1059,  
 730 <https://doi.org/10.1002/2014GB005063>, 2015.  
 731 Henson, S., Le Moigne, F., and Giering, S.: Drivers of Carbon Export Efficiency in the Global Ocean, *Glob.*  
 732 *Biogeochem. Cycles*, 33, 891–903, <https://doi.org/10.1029/2018GB006158>, 2019.  
 733 Henson, S. A., Yool, A., and Sanders, R.: Variability in efficiency of particulate organic carbon export: A model  
 734 study, *Glob. Biogeochem. Cycles*, 29, 33–45, <https://doi.org/10.1002/2014GB004965>, 2015.  
 735 Hernández-Carrasco, I., Orfila, A., Rossi, V., and Garçon, V.: Effect of small scale transport processes on  
 736 phytoplankton distribution in coastal seas, *Sci. Rep.*, 8, 8613, <https://doi.org/10.1038/s41598-018-26857-9>, 2018.  
 737 Heukamp, F. O., Brandt, P., Dengler, M., Tuchen, F. P., McPhaden, M. J., and Moum, J. N.: Tropical Instability  
 738 Waves and Wind-Forced Cross-Equatorial Flow in the Central Atlantic Ocean, *Geophys. Res. Lett.*, 49,  
 739 e2022GL099325, <https://doi.org/10.1029/2022GL099325>, 2022.  
 740 Hidaka, K., Kawaguchi, K., Murakami, M., and Takahashi, M.: Downward transport of organic carbon by diel  
 741 migratory micronekton in the western equatorial Pacific: its quantitative and qualitative importance, 2001.  
 742 Huang, B., Liu, C., Banzon, V., Freeman, E., Graham, G., Hankins, B., Smith, T., and Zhang, H.-M.: Improvements  
 743 of the Daily Optimum Interpolation Sea Surface Temperature (DOISST) Version 2.1, *J. Clim.*, 34, 2923–2939,

<https://doi.org/10.1175/JCLI-D-20-0166.1>, 2021.

Hummels, R., Dengler, M., and Bourlès, B.: Seasonal and regional variability of upper ocean diapycnal heat flux in the Atlantic cold tongue, *Prog. Oceanogr.*, 111, 52–74, <https://doi.org/10.1016/j.pocean.2012.11.001>, 2013.

Inoue, R., Lien, R., Moum, J. N., Perez, R. C., and Gregg, M. C.: Variations of Equatorial Shear, Stratification, and Turbulence Within a Tropical Instability Wave Cycle, *J. Geophys. Res. Oceans*, 124, 1858–1875, <https://doi.org/10.1029/2018JC014480>, 2019.

Irigoien, X., Klevjer, T. A., Røstad, A., Martinez, U., Boyra, G., Acuña, J. L., Bode, A., Echevarria, F., Gonzalez-Gordillo, J. I., Hernandez-Leon, S., Agusti, S., Aksnes, D. L., Duarte, C. M., and Kaartvedt, S.: Large mesopelagic fishes biomass and trophic efficiency in the open ocean, *Nat. Commun.*, 5, 3271, <https://doi.org/10.1038/ncomms4271>, 2014.

Jackson, G. A.: A model of the formation of marine algal flocs by physical coagulation processes, *Deep Sea Res. Part Oceanogr. Res. Pap.*, 37, 1197–1211, [https://doi.org/10.1016/0198-0149\(90\)90038-W](https://doi.org/10.1016/0198-0149(90)90038-W), 1990.

Jouanno, J., Marin, F., Du Penhoat, Y., Sheinbaum, J., and Molines, J.-M.: Seasonal heat balance in the upper 100 m of the equatorial Atlantic Ocean, *J. Geophys. Res.*, 116, C09003, <https://doi.org/10.1029/2010JC006912>, 2011.

Kiko, R., Biastoch, A., Brandt, P., Cravatte, S., Hauss, H., Hummels, R., Kriest, I., Marin, F., McDonnell, A. M. P., Oschlies, A., Picheral, M., Schwarzkopf, F. U., Thurnherr, A. M., and Stemmann, L.: Biological and physical influences on marine snowfall at the equator, *Nat. Geosci.*, 10, 852–858, <https://doi.org/10.1038/ngeo3042>, 2017.

Kiko, R., Brandt, P., Christiansen, S., Faustmann, J., Kriest, I., Rodrigues, E., Schütte, F., and Hauss, H.: Zooplankton-Mediated Fluxes in the Eastern Tropical North Atlantic, *Front. Mar. Sci.*, 7, 358, <https://doi.org/10.3389/fmars.2020.00358>, 2020.

Kiko, R., Picheral, M., Antoine, D., Babin, M., Berline, L., Biard, T., Boss, E., Brandt, P., Carlotti, F., Christiansen, S., Coppola, L., De La Cruz, L., Diamond-Riquier, E., Durrieu De Madron, X., Elineau, A., Gorsky, G., Guidi, L., Hauss, H., Irisson, J.-O., Karp-Boss, L., Karstensen, J., Kim, D., Lekanoff, R. M., Lombard, F., Lopes, R. M., Marec, C., McDonnell, A. M. P., Niemeyer, D., Noyon, M., O'Daly, S. H., Ohman, M. D., Pretty, J. L., Rogge, A., Searson, S., Shibata, M., Tanaka, Y., Tanhua, T., Taucher, J., Trudnowska, E., Turner, J. S., Waite, A., and Stemmann, L.: A global marine particle size distribution dataset obtained with the Underwater Vision Profiler 5, *Earth Syst. Sci. Data*, 14, 4315–4337, <https://doi.org/10.5194/essd-14-4315-2022>, 2022.

Klaas, C. and Archer, D. E.: Association of sinking organic matter with various types of mineral ballast in the deep sea: Implications for the rain ratio, *Glob. Biogeochem. Cycles*, 16, <https://doi.org/10.1029/2001gb001765>, 2002.

Koestner, D., Stramski, D., and Reynolds, R. A.: A Multivariable Empirical Algorithm for Estimating Particulate Organic Carbon Concentration in Marine Environments From Optical Backscattering and Chlorophyll-a Measurements, *Front. Mar. Sci.*, 9, 941950, <https://doi.org/10.3389/fmars.2022.941950>, 2022.

Kriest, I.: Different parameterizations of marine snow in a 1D-model and their influence on representation of marine snow, nitrogen budget and sedimentation, *Deep Sea Res. Part Oceanogr. Res. Pap.*, 49, 2133–2162, [https://doi.org/10.1016/S0967-0637\(02\)00127-9](https://doi.org/10.1016/S0967-0637(02)00127-9), 2002.

Lampitt, R. S., Wishner, K. F., Turley, C. M., and Angel, M. V.: Marine snow studies in the Northeast Atlantic Ocean: distribution, composition and role as a food source for migrating plankton, *Mar. Biol.*, 116, 689–702, <https://doi.org/10.1007/BF00355486>, 1993.

Lee, S., Lopez, H., Tuchen, F. P., Kim, D., Foltz, G. R., and Wittenberg, A. T.: On the Genesis of the 2021 Atlantic Niño, *Geophys. Res. Lett.*, 50, e2023GL104452, <https://doi.org/10.1029/2023GL104452>, 2023.



Longhurst, A.: Seasonal cooling and blooming in tropical oceans, *Deep Sea Res. Part Oceanogr. Res. Pap.*, 40, 2145–2165, [https://doi.org/10.1016/0967-0637\(93\)90095-K](https://doi.org/10.1016/0967-0637(93)90095-K), 1993.

Loukos, H. and Mémery, L.: Simulation of the nitrate seasonal cycle in the equatorial Atlantic Ocean during 1983 and 1984, *J. Geophys. Res. Oceans*, 104, 15549–15573, <https://doi.org/10.1029/1999JC900084>, 1999.

Martin, J. H., Knauer, G. A., Karl, D. M., and Broenkow, W. W.: VERTEX: carbon cycling in the northeast Pacific, *Deep Sea Res. Part Oceanogr. Res. Pap.*, 34, 267–285, [https://doi.org/10.1016/0198-0149\(87\)90086-0](https://doi.org/10.1016/0198-0149(87)90086-0), 1987.

Menkes, C. E., Kennan, S., Flament, P., Dandonneau, Y., Masson, S., Biessy, B., Marchal, E., and Eldin, G.: A whirling ecosystem in the equatorial Atlantic, *Geophys. Res. Lett.*, 29, 1553, <https://doi.org/10.1029/2001GL014576>, 2002.

Moore, C. M., Mills, M. M., Arrigo, K. R., Berman-Frank, I., Bopp, L., Boyd, P. W., Galbraith, E. D., Geider, R. J., Guieu, C., Jaccard, S. L., Jickells, T. D., La Roche, J., Lenton, T. M., Mahowald, N. M., Marañón, E., Marinov, I., Moore, J. K., Nakatsuka, T., Oschlies, A., Saito, M. A., Thingstad, T. F., Tsuda, A., and Ulloa, O.: Processes and patterns of oceanic nutrient limitation, *Nat. Geosci.*, 6, 701–710, <https://doi.org/10.1038/ngeo1765>, 2013.

Moum, J. N., Lien, R.-C., Perlin, A., Nash, J. D., Gregg, M. C., and Wiles, P. J.: Sea surface cooling at the Equator by subsurface mixing in tropical instability waves, *Nat. Geosci.*, 2, 761–765, <https://doi.org/10.1038/ngeo657>, 2009.

Okumura, Y. and Xie, S.-P.: Some Overlooked Features of Tropical Atlantic Climate Leading to a New Niño-Like Phenomenon\*, *J. Clim.*, 19, 5859–5874, <https://doi.org/10.1175/JCLI3928.1>, 2006.

Olivier, L., Reverdin, G., Hasson, A., and Boutin, J.: Tropical Instability Waves in the Atlantic Ocean: Investigating the Relative Role of Sea Surface Salinity and Temperature From 2010 to 2018, *J. Geophys. Res. Oceans*, 125, e2020JC016641, <https://doi.org/10.1029/2020JC016641>, 2020.

Omand, M. M., D’Asaro, E. A., Lee, C. M., Perry, M. J., Briggs, N., Cetinić, I., and Mahadevan, A.: Eddy-driven subduction exports particulate organic carbon from the spring bloom, *Science*, 348, 222–225, <https://doi.org/10.1126/science.1260062>, 2015.

Owens, S. A., Pike, S., and Buesseler, K. O.: Thorium-234 as a tracer of particle dynamics and upper ocean export in the Atlantic Ocean, *Deep Sea Res. Part II Top. Stud. Oceanogr.*, 116, 42–59, <https://doi.org/10.1016/j.dsr2.2014.11.010>, 2015.

Packard, T. T. and Gómez, M.: Modeling vertical carbon flux from zooplankton respiration, *Prog. Oceanogr.*, 110, 59–68, <https://doi.org/10.1016/j.pocean.2013.01.003>, 2013.

Picheral, M., Guidi, L., Stemmann, L., Karl, D. M., Iddaoud, G., and Gorsky, G.: The Underwater Vision Profiler 5: An advanced instrument for high spatial resolution studies of particle size spectra and zooplankton, *Limnol. Oceanogr. Methods*, 8, 462–473, <https://doi.org/10.4319/lom.2010.8.462>, 2010.

Picheral, M., Colin, S., and Irisson, J. O.: EcoTaxa, a tool for the taxonomic classification of images, 2017.

Picheral, M., Catalano, C., Brousseau, D., Claustre, H., Coppola, L., Leymarie, E., Coindat, J., Dias, F., Fevre, S., Guidi, L., Irisson, J. O., Legendre, L., Lombard, F., Mortier, L., Penkerch, C., Rogge, A., Schmechtig, C., Thibault, S., Tixier, T., Waite, A., and Stemmann, L.: The Underwater Vision Profiler 6: an imaging sensor of particle size spectra and plankton, for autonomous and cabled platforms, *Limnol. Oceanogr. Methods*, 20, 115–129, <https://doi.org/10.1002/lom3.10475>, 2022.

Ploug, H. and Grossart, H.: Bacterial growth and grazing on diatom aggregates: Respiratory carbon turnover as a function of aggregate size and sinking velocity, *Limnol. Oceanogr.*, 45, 1467–1475,

824 <https://doi.org/10.4319/lo.2000.45.7.1467>, 2000.

825 Radenac, M.-H., Jouanno, J., Tchamabi, C. C., Awo, M., Bourlès, B., Arnault, S., and Aumont, O.: Physical drivers  
826 of the nitrate seasonal variability in the Atlantic cold tongue, *Biogeosciences*, 17, 529–545,  
827 <https://doi.org/10.5194/bg-17-529-2020>, 2020.

828 Ramondenc, S., Madeleine, G., Lombard, F., Santinelli, C., Stemmann, L., Gorsky, G., and Guidi, L.: An initial  
829 carbon export assessment in the Mediterranean Sea based on drifting sediment traps and the Underwater Vision  
830 Profiler data sets, *Deep Sea Res. Part Oceanogr. Res. Pap.*, 117, 107–119,  
831 <https://doi.org/10.1016/j.dsr.2016.08.015>, 2016.

832 Rodionov, S. N.: A sequential algorithm for testing climate regime shifts, *Geophys. Res. Lett.*, 31, 2004GL019448,  
833 <https://doi.org/10.1029/2004GL019448>, 2004.

834 Rodionov, S. N.: Use of prewhitening in climate regime shift detection, *Geophys. Res. Lett.*, 33, 2006GL025904,  
835 <https://doi.org/10.1029/2006GL025904>, 2006.

836 ~~Schott, F. A., Fischer, J., and Stramma, L.: Transports and Pathways of the Upper-Layer Circulation in the Western~~  
837 ~~Tropical Atlantic, *J. Phys. Oceanogr.*, 28, 1904–1928, <https://doi.org/10.1175/1520-0485.1998>, 1998.~~

838 Ser-Giacomi, E., Baudena, A., Rossi, V., Follows, M., Clayton, S., Vasile, R., López, C., and Hernández-García,  
839 E.: Lagrangian betweenness as a measure of bottlenecks in dynamical systems with oceanographic examples, *Nat.*  
840 *Commun.*, 12, 4935, <https://doi.org/10.1038/s41467-021-25155-9>, 2021.

841 Sherman, J., Subramaniam, A., Gorbunov, M. Y., Fernández-Carrera, A., Kiko, R., Brandt, P., and Falkowski, P.  
842 G.: The Photophysiological Response of Nitrogen-Limited Phytoplankton to Episodic Nitrogen Supply Associated  
843 With Tropical Instability Waves in the Equatorial Atlantic, *Front. Mar. Sci.*, 8, 814663,  
844 <https://doi.org/10.3389/fmars.2021.814663>, 2022.

845 Shi, W. and Wang, M.: Tropical instability wave modulation of chlorophyll-a in the Equatorial Pacific, *Sci. Rep.*,  
846 11, 22517, <https://doi.org/10.1038/s41598-021-01880-5>, 2021.

847 Siegel, D. A., Burd, A. B., Estapa, M., Fields, E., Johnson, L., Romanelli, E., Brzezinski, M. A., Buesseler, K. O.,  
848 Clevenger, S., Cetinić, I., Drago, L., Durkin, C. A., Kiko, R., Kramer, S. J., Maas, A., Omand, M., Passow, U., and  
849 Steinberg, D. K.: 10 Dynamics of Aggregates and Sinking Carbon Fluxes in a 11 Turbulent Ocean 12 Draft: April  
850 22, 2024, n.d.

851 Song, Q., Tang, Y., and Aiki, H.: Dual Wave Energy Sources for the Atlantic Niño Events Identified by Wave  
852 Energy Flux in Case Studies, *J. Geophys. Res. Oceans*, 128, e2023JC019972,  
853 <https://doi.org/10.1029/2023JC019972>, 2023.

854 Steinberg, D. K. and Landry, M. R.: Zooplankton and the Ocean Carbon Cycle, *Annu. Rev. Mar. Sci.*, 9, 413–444,  
855 <https://doi.org/10.1146/annurev-marine-010814-015924>, 2017.

856 Stemmann, L. and Boss, E.: Plankton and Particle Size and Packaging: From Determining Optical Properties to  
857 Driving the Biological Pump, *Annu. Rev. Mar. Sci.*, 4, 263–290, <https://doi.org/10.1146/annurev-marine-120710-100853>, 2012.

858 Stemmann, L., Gorsky, G., Marty, J.-C., Picheral, M., and Miquel, J.-C.: Four-year study of large-particle vertical  
859 distribution (0–1000m) in the NW Mediterranean in relation to hydrology, phytoplankton, and vertical flux, *Deep*  
860 *Sea Res. Part II Top. Stud. Oceanogr.*, 49, 2143–2162, [https://doi.org/10.1016/S0967-0645\(02\)00032-2](https://doi.org/10.1016/S0967-0645(02)00032-2), 2002.

861 Stemmann, L., Jackson, G. A., and Ianson, D.: A vertical model of particle size distributions and fluxes in the  
862 midwater column that includes biological and physical processes—Part I: model formulation, *Deep Sea Res. Part*  
863

**Deleted:** Schott, F. A., Fischer, J., and Stramma, L.:  
Transports and Pathways of the Upper-Layer Circulation in  
the Western Tropical Atlantic, *J. Phys. Oceanogr.*, 28, 1904–  
1928, <https://doi.org/10.1175/1520-0485.1998>.

868 Oceanogr. Res. Pap., 51, 865–884, <https://doi.org/10.1016/j.dsr.2004.03.001>, 2004a.

869 Stemmann, L., Jackson, G. A., and Gorsky, G.: A vertical model of particle size distributions and fluxes in the  
870 midwater column that includes biological and physical processes—Part II: application to a three year survey in the  
871 NW Mediterranean Sea, Deep Sea Res. Part Oceanogr. Res. Pap., 51, 885–908,  
872 <https://doi.org/10.1016/j.dsr.2004.03.002>, 2004b.

873 Tréguer, P., Bowler, C., Moriceau, B., Dutkiewicz, S., Gehlen, M., Aumont, O., Bittner, L., Dugdale, R., Finkel,  
874 Z., Iudicone, D., Jahn, O., Guidi, L., Lasbleiz, M., Leblanc, K., Levy, M., and Pondaven, P.: Influence of diatom  
875 diversity on the ocean biological carbon pump, Nat. Geosci., 11, 27–37, <https://doi.org/10.1038/s41561-017-0028->  
876 x, 2018.

877 Trudnowska, E., Lacour, L., Ardyna, M., Rogge, A., Irisson, J. O., Waite, A. M., Babin, M., and Stemmann, L.:  
878 Marine snow morphology illuminates the evolution of phytoplankton blooms and determines their subsequent  
879 vertical export, Nat. Commun., 12, 2816, <https://doi.org/10.1038/s41467-021-22994-4>, 2021.

880 Tuchen, F. P., Perez, R. C., Foltz, G. R., Brandt, P., and Lumpkin, R.: Multidecadal Intensification of Atlantic  
881 Tropical Instability Waves, Geophys. Res. Lett., 49, e2022GL101073, <https://doi.org/10.1029/2022GL101073>,  
882 2022.

883 Tuchen, F. P., Perez, R. C., Foltz, G. R., Brandt, P., Subramaniam, A., Lee, S., Lumpkin, R., and Hummels, R.:  
884 Modulation of Equatorial Currents and Tropical Instability Waves During the 2021 Atlantic Niño, J. Geophys. Res.  
885 Oceans, 129, e2023JC020431, <https://doi.org/10.1029/2023JC020431>, 2024.

886 Turner, J. T.: Zooplankton fecal pellets, marine snow, phytodetritus and the ocean’s biological pump, Prog.  
887 Oceanogr., 130, 205–248, <https://doi.org/10.1016/j.pocean.2014.08.005>, 2015.

888 Villareal, T. A., Adornato, L., Wilson, C., and Schoenbaechler, C. A.: Summer blooms of diatom-diazotroph  
889 assemblages and surface chlorophyll in the North Pacific gyre: A disconnect, J. Geophys. Res., 116, C03001,  
890 <https://doi.org/10.1029/2010JC006268>, 2011.

891 Warner, S. J., Holmes, R. M., M. Hawkins, E. H., S. Hoecker-Martínez, M., Savage, A. C., and Moum, J. N.:  
892 Buoyant Gravity Currents Released from Tropical Instability Waves, J. Phys. Oceanogr., 48, 361–382,  
893 <https://doi.org/10.1175/JPO-D-17-0144.1>, 2018.

894 Wefer, G. and Fischer, G.: Seasonal patterns of vertical particle flux in equatorial and coastal upwelling areas of  
895 the eastern Atlantic, Deep Sea Res. Part Oceanogr. Res. Pap., 40, 1613–1645, <https://doi.org/10.1016/0967->  
896 0637(93)90019-Y, 1993.

897 Yool, A., Popova, E. E., and Anderson, T. R.: MEDUSA-2.0: an intermediate complexity biogeochemical model  
898 of the marine carbon cycle for climate change and ocean acidification studies, Geosci. Model Dev., 6, 1767–1811,  
899 <https://doi.org/10.5194/gmd-6-1767-2013>, 2013.